

MoS₂ nanoflowers consisting of nanosheets with a controllable interlayer distance as high-performance lithium ion battery anodes

Yutao Lu,^{ab} Xiayin Yao,^{*a} Jingyun Yin,^a Gang Peng,^a Ping Cui^a and Xiaoxiong Xu^{*a}

MoS₂ nanoflowers consisting of nanosheets are synthesized by a one-step hydrothermal method. The interlayer distances of the MoS₂ nanosheets, accompanied with the changes of crystallinity, defects, specific surface areas as well as the thickness of the MoS₂ nanosheets, can be well controlled via simply altering hydrothermal reaction temperatures. The effect of interlayer distances on the lithium storage capability for lithium ion batteries is investigated. The results show that MoS₂ synthesized under 200 °C with an interlayer distance of 0.65 nm exhibit the highest lithium storage capacity and the best rate capability, showing a high discharge capacity of 814.2 mA h g⁻¹ at 100 mA g⁻¹ after 50 cycles and as high as 652.2 mA h g⁻¹ and 547.3 mA h g⁻¹ at current densities of 1 A g⁻¹ and 2 A g⁻¹ at 25 °C, respectively. The excellent lithium storage properties of the resultant MoS₂ nanoflowers are attributed to its controllable optimized interplanar distance with good crystallinity, appropriate surface area and defects as well as thickness of the nanosheets.

Introduction

Lithium ion batteries are the main power sources for portable electronic devices and are considered to be one of the leading candidates for powering hybrid electric vehicles and electric vehicles.^{1,2} Graphite, a commonly used anode material in commercial lithium ion batteries, cannot meet the requirement of future energy storage systems due to its limited theoretical capacity (372 mA h g⁻¹).² To address this problem, great efforts have been conducted to develop new electrode materials.³⁻⁸ Recently, metal sulfides, such as SnS₂, WS₂, CoS₂, FeS₂, CuS, NiS₂ and MoS₂, have been extensively investigated as anode materials.⁹⁻¹⁶ Among them, MoS₂ has received particular attention in the merit of its high lithium ion capacity and structure stability. It can react with four lithium ions per formula unit by conversion mechanism, forming Mo nanoparticles and insoluble Li₂S matrix and giving a 670 mA h g⁻¹ lithium storage capacity, one and half time higher than current graphite anode.¹⁷

However, MoS₂ generally suffers from fast capacity fading, poor rate capability due to volume changes during repeat cycles and formation of a thick gel-like polymeric layer inhibiting successive lithiation-delithiation reactions.¹⁸ These problem can be partly solved through preparing MoS₂-based nanocomposites with carbonaceous materials¹⁸⁻²¹ or using

nanostructured MoS₂ electrode with enlarged interlayer distances to facilitate lithium ion intercalation.^{19,22-25} As reported that when a lithium ion intercalates into layered MoS₂, it enters the S layer and forms Li-S bonds, resulting in volume changes.²² Increasing the interlayer distance of MoS₂ can provide larger space for lithium ion to intercalate, which also reduces the barriers to lithium ion mobility, thereby facilitating lithium ion diffusion. Du *et al.* prepared restacked MoS₂ with enlarged *c* lattice parameter and surface area by exfoliation and restacking process and found that the obtained MoS₂ exhibits high reversible lithium storage capacity and superior rate capability as anode material for lithium ion batteries.²² However, up to now, the effect of different interlayer distances on the electrochemical performances is still not well understood.

Herein, a simple hydrothermal method was used to prepare a series of MoS₂ flowers with different interlayer spacing ranged from 0.63 nm to 0.70 nm. The resultant MoS₂ flowers were employed as anode materials for lithium ion batteries and the effect of interlayer spacing on electrochemical properties was systematically investigated. The results show that the MoS₂ flowers consisting of nanosheets with optimized interlayer distance of 0.65 nm and good crystallinity, appropriate surface area and defects as well as thickness of nanosheets exhibit the highest lithium storage capacity and the best rate capability.

Experimental

All the chemicals were analytical grade and used without further purification. MoS₂ nanoflowers were prepared by a facile

^aNingbo Institute of Materials Technology and Engineering, Chinese Academy of Sciences, Ningbo, 315201, P. R. China. E-mail: xuxx@nimte.ac.cn; yaoxy@nimte.ac.cn

^bFaculty of Materials Science and Chemical Engineering, Ningbo University, Ningbo 315211, P. R. China

hydrothermal process. In detail, 1.07 g ammonium molybdate ($(\text{NH}_4)_6\text{Mo}_7\text{O}_{24} \cdot 4\text{H}_2\text{O}$) and 0.93 g thiourea ($\text{CS}(\text{NH}_2)_2$) were dissolved in 70 mL de-ionized water under vigorous stirring. After stirring for 1 h, the transparent solution was transferred into a 100 mL Teflon-lined stainless steel autoclave. Then the autoclave was sealed and heated to 160–220 °C for 24 h. After that, the autoclave was cooled to room temperature. The black products deposited at the bottom were filtrated, washed with de-ionized water for three times and dried in vacuum oven at 100 °C for 12 h. The sample synthesized at 160, 180, 200 and 220 °C were labeled as MoS_2 -160, MoS_2 -180, MoS_2 -200, MoS_2 -220, respectively.

The structure of as-prepared samples was characterized by X-ray powder diffraction (XRD) (German Bruker D8) with Cu-K α radiation at a voltage of 40 kV and a current of 40 mA. The morphology and particle size were observed by field emission scanning electron microscope (FESEM, S-4800, Hitachi) and high-resolution transmission electron microscopy (HRTEM) (Tecnai F20, FEI). Different metal-sulfur vibration modes were obtained using a Raman spectrometer (Renishaw, invia-reflex). The surface areas were tested by nitrogen adsorption-desorption analysis (Micromeritics ASAP 2020M).

Electrochemical properties of the MoS_2 electrodes were measured with CR2032 coin cells. The electrode was prepared by spreading a mixture of active material (80 wt%), acetylene black (10 wt%) and carboxyl methyl cellulose binder (10 wt%) dissolved in de-ionized water onto a copper foil current collector and then dried in vacuum. The electrode was separated from lithium foil by a Celgard 2502 separator. The electrolyte (Guangzhou Tianci Materials Technology Co, Ltd.) was 1 M LiPF_6 dissolved into a mixture of EC/DMC/DEC (1 : 1 : 1, v/v/v). The galvanostatic charge and discharge tests were carried out on a LAND-CT2001A battery tester (Jinnuo Wuhan Co. Ltd P. R. China) between 0.01 V and 3.0 V. Cyclic voltammetry and electrochemical impedance spectroscopy were tested on Solartron 1470E multi-channel potentiostats. Cyclic voltammetry curves were obtained between 0.01 V and 3.0 V with a scan rate of 0.2 mV s^{-1} . Electrochemical impedance spectroscopy (EIS) was carried out on the cycled batteries charged to 3.0 V with the frequency range of 1 MHz to 0.1 Hz and RMS potential of 10 mV. All the electrochemical measurements were tested at a constant temperature of 25 °C.

Results and discussion

Fig. 1 shows the XRD patterns of the as-synthesized MoS_2 samples. The main diffraction peaks of all samples are at $2\theta = 14.2^\circ$, 33.6° , 39.8° and 59.3° , which are corresponding to (002), (100), (103) and (110) planes of MoS_2 and can be indexed to orthorhombic phase of MoS_2 (JCPDS no. 37-1492). No diffraction peaks from residues or impurities have been detected, indicating the high purity of the products. With the increasing hydrothermal temperatures, the intensity of diffraction peaks becomes sharper and stronger, indicating the increasement of the crystal sizes and improvement of crystallinity. Meanwhile, the location of (002) peak shift to high angle, which means the decrease of (002) interplanar spacing,²⁶ leading to a smaller

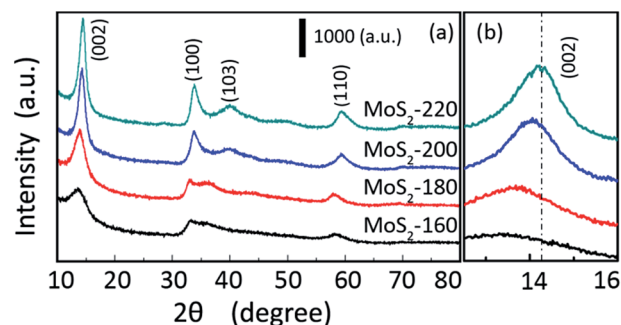


Fig. 1 (a) XRD patterns of four MoS_2 samples. (b) Magnified XRD patterns of MoS_2 samples in 2θ range of 13.0 – 16.0° .

space for Li ions intercalation. Raman analysis shown in Fig. 2 further confirms the formation of MoS_2 . The appearances of two peaks at 378 cm^{-1} (E_{2g}) and 404 cm^{-1} (A_{1g}) are due to the first-order Raman vibration modes within the S–Mo–S layer.^{17,27} It has been reported that the relatively broader as well as weaker intensity of E_{2g} peak suggest that the crystal structure of MoS_2 may contain substantial defect sites.^{28,29} With the hydrothermal temperature increases, the peaks of E_{2g} and A_{1g} become stronger and sharper, indicating a reduction of defects and better crystallinity,²⁹ which is agreed with the XRD results. Besides, the layer number of MoS_2 decreases as well because the frequency of the A_{1g} mode decreases monotonously with increasing hydrothermal temperatures.^{30,31}

The morphologies of the MoS_2 samples were observed using SEM and the results are shown in Fig. 3a–d. All samples obtained show a flower-like morphology with diameters of 400–900 nm and composed of sheet-like subunits in random orientation. The nanosheets, having the thickness of 6–25 nm, aggregate to form the loose flower-like architecture, which are similar to other reported 3D MoS_2 microstructure.^{17,32,33} As the hydrothermal temperature increases, the nanoflowers become fluffy and the nanosheets turn thinner, which is in good agreement with the Raman analysis. The fluffy structure could provide more void space, which could buffer the volume changes during intercalation–deintercalation process.³² The

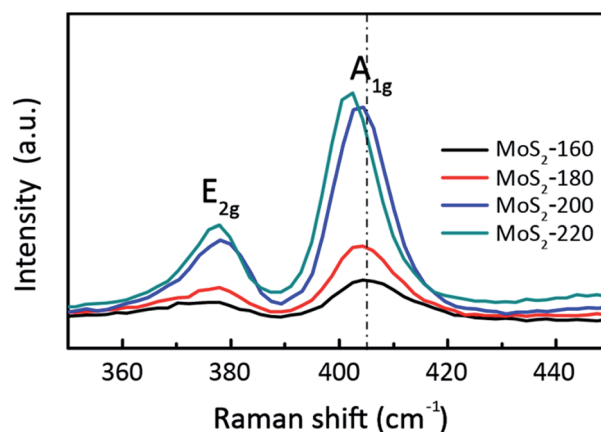


Fig. 2 Raman spectra of the MoS_2 samples.

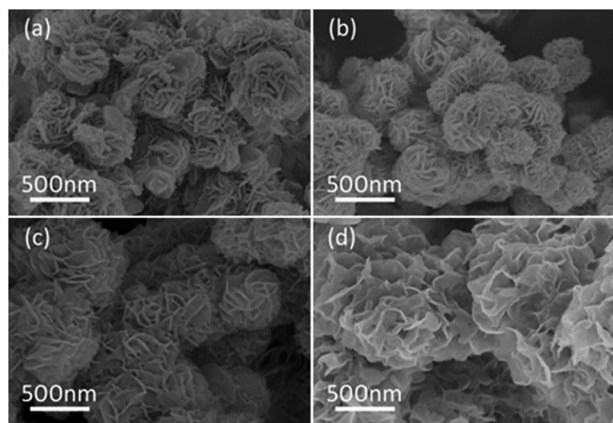


Fig. 3 SEM images of (a) MoS₂-160, (b) MoS₂-180, (c) MoS₂-200, (d) MoS₂-220.

reduction of the thickness of nanosheet could provide short pathways and high kinetics for lithium ion insertion-extraction.^{33,34} Furthermore, the surface area of MoS₂ samples also increases with the reaction temperatures. As determined by Brunauer-Emmett-Teller method, the surface area are found to be 9.68, 15.19, 16.46, 26.25 m² g⁻¹ for the samples synthesized under 160, 180, 200 and 220 °C, respectively. In order to further investigate the structural information of MoS₂, HRTEM were carried, as presented in Fig. 4a-d. It can be obviously seen that the samples consist of few-layered MoS₂ nanosheets. The interlayer distance of (002) plane measured from HRTEM images are 0.70, 0.68, 0.65, 0.63 nm with the increasing hydrothermal temperatures, respectively, which coincide with the results of XRD. It can be clearly seen that MoS₂ nanosheets with various interlayer distance is also accompanied with the

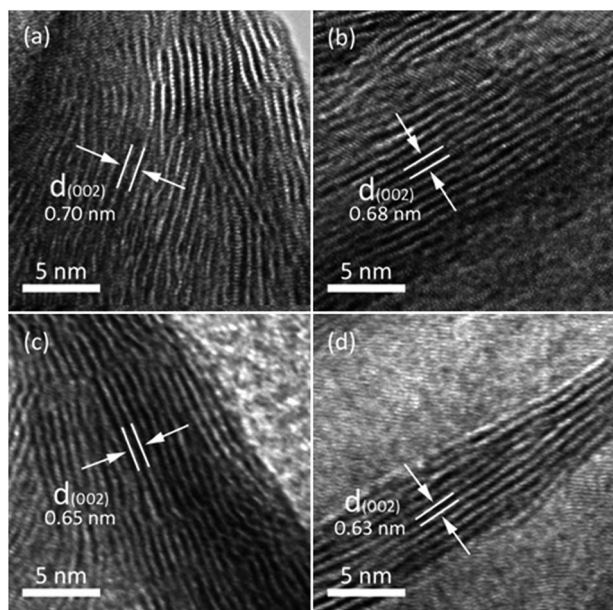


Fig. 4 HRTEM images of (a) MoS₂-160, (b) MoS₂-180, (c) MoS₂-200, (d) MoS₂-220.

changes of their crystallinity, defects, thickness as well as specific surfaces area. The enlarged interlayer distances could facilitate lithium ion intercalation, resulting higher specific capacity.

Cyclic voltammogram (CV) tests for coin cells were recorded at ambient temperature in the voltage range of 0.01–3.0 V at a scan rate of 0.2 mV s⁻¹ for the initial five cycles, as shown in Fig. 5. Here, take MoS₂-200 as an example to elucidate the electrochemical process of the MoS₂ flowers (Fig. 5c). During the first discharge process, two prominent peaks at 0.9 and 0.3 V were observed. The peak at 0.9 V is due to the intercalation of Li-ions in the interlayer spacing of MoS₂ (formation of Li_xMoS₂),^{17,35} changing the MoS₂ structure from 2H (trigonal prismatic) to 1T (octahedral).^{22,36,37} This peak disappears in the samples MoS₂-160 and MoS₂-180 because of their low crystallinity, which are nearly amorphous.³² The peak at 0.3 V is corresponds to the decomposition of Li_xMoS₂ to Mo particles embedded in a Li₂S matrix.^{15,17,20,22,25} In the anodic sweep, two peaks at 1.7 V and 2.3 V were observed, which could be associated with delithiation of Mo and oxidation of Li₂S into sulfur, respectively.³⁸ Therefore, after completion of first cycle, the electrode comprises unreacted MoS₂, Mo, Li, and S.¹⁷ In the following discharge curves, the peak at 0.9 V disappears and the other two peaks at 1.8 and 1.0 V can be observed. The redox of Mo nanoparticles and reversible formation of Li₂S should be the reason for these two peaks.^{39,40} For the other samples, the variation of peaks is attributed to the different electronic environment and different sites or quantity of defects in MoS₂ crystal structure.^{17,40,41}

To determine the lithium storage properties of MoS₂, the galvanostatic charge-discharge tests were carried out under a constant current density between 0.01 V and 3.0 V at 25 °C. Fig. 6 depicts the first, second, fiftieth discharge-charge profiles of the four samples at a current density of 100 mA g⁻¹. The voltage plateaus of lithiation-delithiation curves are agree with the CV results. The initial discharge-charge capacities for MoS₂-160, MoS₂-180, MoS₂-200, MoS₂-220 are 1159.7/962.8, 1112.5/939, 925.9/791.8 and 872.2/725.5 mA h g⁻¹, respectively. The

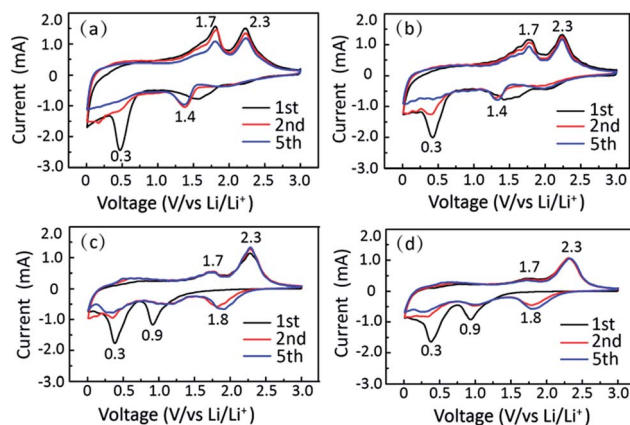


Fig. 5 Cyclic voltammograms of MoS₂ samples at a scan rate of 0.2 mV s⁻¹ in potential range of 3.0 to 0.01 V vs. Li/Li⁺. (a) MoS₂-160, (b) MoS₂-180, (c) MoS₂-200, (d) MoS₂-220.

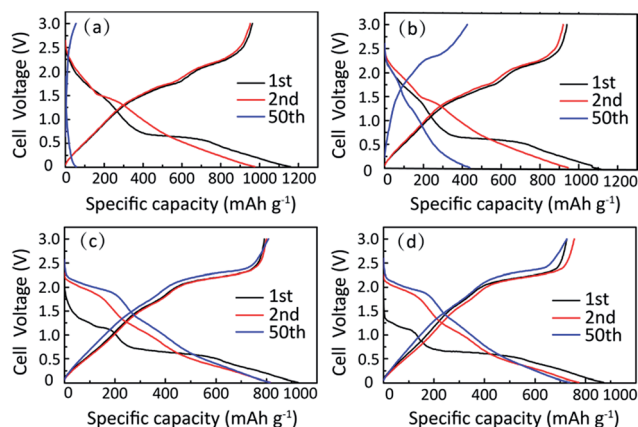


Fig. 6 Discharge-charge profiles of MoS₂ samples at 100 mA g⁻¹ in the potential window of 3.0 to 0.01 V vs. Li/Li⁺. (a) MoS₂-160, (b) MoS₂-180, (c) MoS₂-200, (d) MoS₂-220.

irreversible capacity loss for all the samples in the first cycle may be due to the formation of solid-electrolyte interface (SEI) layer, decomposition of electrolyte, and the trapping of some irreversible lithium inside lattice.^{21,36,39} The difference of their first discharge capacities could be ascribed to their various layer spacing and the quantity of defects. The sample synthesized at lower hydrothermal temperature has larger interlayer spacing and more defects, resulting in enhanced electrochemical performance in terms of the initial lithiation kinetics and the charge storage capacity.^{19,22,42}

Fig.7a gives more information about the cycling performance of MoS₂ samples at a constant current density of 100 mA g⁻¹. The results are listed in Table 1. Clearly, MoS₂-160 and MoS₂-180 suffer a rather rapid capacity fading after 50 cycles. By contrast, the other two samples, *i.e.* MoS₂-200 and MoS₂-220, show significantly improved cycling stability. After 50 cycles, the

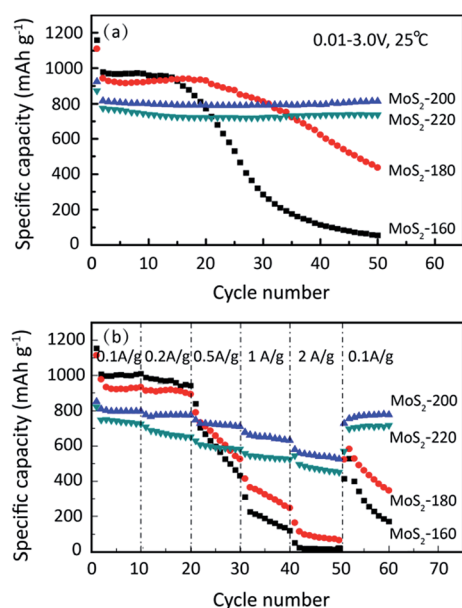


Fig. 7 (a) Cycling performances of MoS₂ samples at 100 mA g⁻¹. (b) Rate performances of MoS₂ samples at different current densities.

reversible capacities are 814.2 mA h g⁻¹ and 736.5 mA h g⁻¹ for MoS₂-200 and MoS₂-220, respectively. The high reversible capacity and cycling durability of sample MoS₂-200 is comparative to those of other reported nanostructured MoS₂ tested under similar conditions.^{17,20} It is generally accepted that MoS₂ with enlarged *c* lattice parameter will exhibit better electrochemical performances as lithium ion battery anodes when the interlayer distance is taken into account alone. In this case, the MoS₂ with interlayer distances of 0.68 nm or 0.70 nm should exhibit higher reversible lithium storage capacity than that with interlayer distances of 0.65 nm. However, the electrochemical performances of MoS₂ not only depend on the interlayer distance but also its crystallinity, defects, thickness as well as specific surface area. The better cyclic performances of sample MoS₂-200 and MoS₂-220 may be attributed to the high crystallinity, which may benefit for their structure stability. Besides, the presence of more void space provide effective buffering for the mechanical stress and volume variation during Li-ions insertion-extraction.^{32,41} Moreover, the flexible nature of the ultrathin MoS₂ nanosheets enhances the robustness of the electrode structure.³² Compared with MoS₂-220, although MoS₂-200 shows lower crystallinity, more defects, smaller specific surface area and thicker nanosheets, it shows enlarged interlayer distance, which could provide larger space for lithium ion to intercalate, resulting in better electrochemical performances.

The rate performance of MoS₂ samples was also investigated under different current densities ranged from 0.1 to 2 A g⁻¹, as show in Fig. 7b. The discharge capacity values at the fifth cycle were selected for each current densities and the results are also listed in Table 1. The reversible discharge capacities for the MoS₂-200 and MoS₂-220 at 0.5, 1.0 and 2.0 A g⁻¹ are 723, 652, 547 and 593, 537, 473 mA h g⁻¹, respectively. Remarkably, stable reversible discharge capacities of 771 and 709 mA h g⁻¹ can be recovered when the current density returns to the 0.1 A g⁻¹. By comparison, the capacities of MoS₂-160 and MoS₂-180 decays rapidly with increasing current density and the capacity values at 0.5, 1.0 and 2.0 A g⁻¹ are only 599, 188, 18 and 660, 328, 87 mA h g⁻¹, respectively. When the current density returns to the 0.1 A g⁻¹, reversible discharge capacities of 290.4 and 463.9 mA h g⁻¹ are obtained, which are much lower than those of MoS₂-200 and MoS₂-220. Obviously, MoS₂ synthesized under high temperatures with smaller interlayer distances show much better electrochemical performances. This could be attributed to their larger surface area and extremely thin nanosheets, which endow the material with dramatic increment of reactive sites and electrode-electrolyte interface, as well as much shorter diffusion pathway, thus enabling efficient Li⁺/electron fast transport.

In order to gain insight into the differences in electrochemical performances of the resultant MoS₂, EIS measurements were carried out after the first cycle and fiftieth cycle. Fig. 8 shows the Nyquist impedance plots of the MoS₂-160 and MoS₂-200 electrodes and the inset in Fig. 8a is the equivalent circuit model^{30,39} used for fitting the experimental EIS data. *R*_e is the internal resistance; the high frequency semicircle corresponds to resistance *R*_f and the constant phase capacitance (CPE₁) of SEI film; the medium frequency semicircle is related with the charge-transfer resistance (*R*_{ct}) and CPE₂ of electrode-

Table 1 Electrochemical performances of MoS₂ samples

Samples	Cycle performances (mA h g ⁻¹ @100 mA g ⁻¹)			Rate performances (mA h g ⁻¹)				
	1st	50th	Retention	0.1 A g ⁻¹	0.2 A g ⁻¹	0.5 A g ⁻¹	1 A g ⁻¹	2 A g ⁻¹
MoS ₂ -160	1159.7	55.7	4.8%	1008.2	965.4	599.0	187.6	17.8
MoS ₂ -180	1112.5	438.7	39.4%	923.7	918.6	659.5	328.1	87.2
MoS ₂ -200	925.9	814.2	87.9%	797.4	773.3	723.1	652.2	547.3
MoS ₂ -220	872.2	736.5	84.4%	740.9	668.7	593.0	536.7	472.8

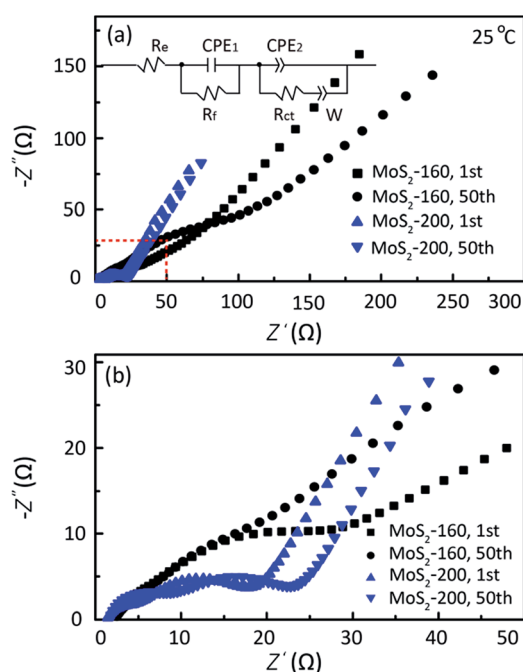


Fig. 8 (a) Nyquist plots of MoS₂-160 and MoS₂-200 with frequency range from 10^6 to 0.1 Hz at the 1st and 50th cycle in the potential window of 3.0 to 0.01 V; the inset in (a) is the equivalent circuit used for fitting the EIS data. (b) Magnification of red square in (a).

electrolyte interface; The straight line in low frequency representing the Warburg resistance (W) is assigned to the Li-ions diffusion in electrode. It can be clearly seen that in the high-to-low frequencies range, MoS₂-200 has lower R_f and R_{ct} values than those of MoS₂-160 after the first and fiftieth cycle; in addition, the charge transfer resistance of MoS₂-160 was significantly increased from 38.3 Ω to 184.4 Ω while MoS₂-200 only slightly changed from 15.3 Ω to 20.7 Ω . This observation confirms that both SEI film resistance and charge-transfer resistance of MoS₂-200 are much smaller than those of MoS₂-160, which gives the evidences for the improvement of rate capability and cycling stability for the MoS₂ samples synthesized under higher hydrothermal temperatures.

Conclusions

MoS₂ nanoflowers consisting of nanosheets have been successfully synthesized by a facile hydrothermal method. The

hydrothermal temperature played an important role in determining the interlayer-spacing of MoS₂ nanosheets. Samples synthesized under lower hydrothermal temperature show enlarged interlayer distance accompany with lower crystallinity, more defects, smaller specific surface area and thicker nanosheets. When employed as anodes for lithium ion batteries, MoS₂ synthesized under 200 °C with an appropriate interlayer distance of 0.65 nm exhibit the highest lithium storage capacity and the best rate capability, showing a high discharge capacity of 814.2 mA h g⁻¹ at 100 mA g⁻¹ after 50 cycles and as high as 652.2 mA h g⁻¹ and 547.3 mA h g⁻¹ at current densities of 1 A g⁻¹ and 2 A g⁻¹ at 25 °C respectively. Clearly, the electrochemical performances of MoS₂ not only depend on the interlayer distance but also its crystallinity, defects, thickness as well as specific surface area. The excellent lithium storage properties are attributed to its controllable optimized interplanar distance with good crystallinity, appropriate surface area and defects as well as thickness of nanosheets, which could benefit for lithium-ion to intercalate and accommodate volume changes while keeping its structure stability, providing more reaction sites and offering short pathways and high kinetics for lithium ion insertion-extraction.

Acknowledgements

The authors are grateful for financial support from the National Key Basic Research Program of China (973 Program, Grant no. 2012CB722700), the National Natural Science Foundation of China (Grant no. 51172250, 51202265), the Strategic Priority Research Program of the Chinese Academy of Sciences, (Grant no. XDA09010201) and the Key Research Program of the Chinese Academy of Sciences, (Grant no. KGZD-EW-202).

Notes and references

- 1 P. G. Bruce, B. Scrosati and J. M. Tarascon, *Angew. Chem., Int. Ed.*, 2008, **47**, 2930–2946.
- 2 L. Ji, Z. Lin, M. Alcoutlabi and X. Zhang, *Energy Environ. Sci.*, 2011, **4**, 2682.
- 3 C. Yuan, H. B. Wu, Y. Xie and X. W. Lou, *Angew. Chem., Int. Ed.*, 2014, **53**, 1488–1504.
- 4 M. V. Reddy, G. V. Subba Rao and B. V. R. Chowdari, *Chem. Rev.*, 2013, **113**, 5364–5457.
- 5 D. Ma, Z. Cao and A. Hu, *Nano-Micro Lett.*, 2014, **6**, 347–358.

- 6 Q. Gao, L. Yang, X. Lu, J. Mao, Y. Zhang, Y. Wu and Y. Tang, *J. Mater. Chem.*, 2010, **20**, 2807.
- 7 L. Yang, L. Liu, Y. Zhu, X. Wang and Y. Wu, *J. Mater. Chem.*, 2012, **22**, 13148.
- 8 L. C. Yang, Q. S. Gao, Y. Tang, Y. P. Wu and R. Holze, *J. Power Sources*, 2008, **179**, 357–360.
- 9 B. Luo, Y. Fang, B. Wang, J. Zhou, H. Song and L. Zhi, *Energy Environ. Sci.*, 2012, **5**, 5226.
- 10 C. Feng, L. Huang, Z. Guo and H. Liu, *Electrochem. Commun.*, 2007, **9**, 119–122.
- 11 Q. Wang, L. Jiao, Y. Han, H. Du, W. Peng, Q. Huan, D. Song, Y. Si, Y. Wang and H. Yuan, *J. Phys. Chem. C*, 2011, **115**, 8300–8304.
- 12 D. Zhang, J. P. Tu, J. Y. Xiang, Y. Q. Qiao, X. H. Xia, X. L. Wang and C. D. Gu, *Electrochim. Acta*, 2011, **56**, 9980–9985.
- 13 Y. Han, Y. Wang, W. Gao, Y. Wang, L. Jiao, H. Yuan and S. Liu, *Powder Technol.*, 2011, **212**, 64–68.
- 14 W. Ni, B. Wang, J. Cheng, X. Li, Q. Guan, G. Gu and L. Huang, *Nanoscale*, 2014, **6**, 2618.
- 15 M. Wang, G. Li, H. Xu, Y. Qian and J. Yang, *ACS Appl. Mater. Interfaces*, 2013, **5**, 1003–1008.
- 16 X. Huang, Z. Zeng and H. Zhang, *Chem. Soc. Rev.*, 2013, **42**, 1934.
- 17 U. K. Sen and S. Mitra, *ACS Appl. Mater. Interfaces*, 2013, **5**, 1240–1247.
- 18 S. K. Das, R. Mallavajula, N. Jayaprakash and L. A. Archer, *J. Mater. Chem.*, 2012, **22**, 12988.
- 19 X. Zhou, L. J. Wan and Y. G. Guo, *Nanoscale*, 2012, **4**, 5868–5871.
- 20 C. Zhang, H. B. Wu, Z. Guo and X. W. Lou, *Electrochem. Commun.*, 2012, **20**, 7–10.
- 21 C. Zhu, X. Mu, P. A. van Aken, Y. Yu and J. Maier, *Angew. Chem., Int. Ed.*, 2014, **53**, 2152–2156.
- 22 G. Du, Z. Guo, S. Wang, R. Zeng, Z. Chen and H. Liu, *Chem. Commun.*, 2010, **46**, 1106–1108.
- 23 H. Liu, D. Su, R. Zhou, B. Sun, G. Wang and S. Z. Qiao, *Adv. Energy Mater.*, 2012, **2**, 970–975.
- 24 J. Xiao, D. Choi, L. Cosimbescu, P. Koech, J. Liu and J. P. Lemmon, *Chem. Mater.*, 2010, **22**, 4522–4524.
- 25 H. Hwang, H. Kim and J. Cho, *Nano Lett.*, 2011, **11**, 4826–4830.
- 26 N. Li, Y. Chai, Y. Li, Z. Tang, B. Dong, Y. Liu and C. Liu, *Mater. Lett.*, 2012, **66**, 236–238.
- 27 B. C. Windom, W. G. Sawyer and D. W. Hahn, *Tribol. Lett.*, 2011, **42**, 301–310.
- 28 K. K. Liu, W. Zhang, Y. H. Lee, Y. C. Lin, M. T. Chang, C. Y. Su, C. S. Chang, H. Li, Y. Shi, H. Zhang, C. S. Lai and L. J. Li, *Nano Lett.*, 2012, **12**, 1538–1544.
- 29 D. Wang, Z. Pan, Z. Wu, Z. Wang and Z. Liu, *J. Power Sources*, 2014, **264**, 229–234.
- 30 Z. Wang, T. Chen, W. Chen, K. Chang, L. Ma, G. Huang, D. Chen and J. Y. Lee, *J. Mater. Chem. A*, 2013, **1**, 2202.
- 31 H. Li, Q. Zhang, C. C. R. Yap, B. K. Tay, T. H. T. Edwin, A. Olivier and D. Baillargeat, *Adv. Funct. Mater.*, 2012, **22**, 1385–1390.
- 32 S. Ding, D. Zhang, J. S. Chen and X. W. Lou, *Nanoscale*, 2012, **4**, 95–98.
- 33 S. Liang, J. Zhou, J. Liu, A. Pan, Y. Tang, T. Chen and G. Fang, *CrystEngComm*, 2013, **15**, 4998.
- 34 D. Rangappa, K. D. Murukanahally, T. Tomai, A. Unemoto and I. Honma, *Nano Lett.*, 2012, **12**, 1146–1151.
- 35 S. Hu, W. Chen, J. Zhou, F. Yin, E. Uchaker, Q. Zhang and G. Cao, *J. Mater. Chem. A*, 2014, **2**, 7862.
- 36 Y. Liu, L. Ren, X. Qi, L. Yang, J. Li, Y. Wang and J. Zhong, *J. Energy Chem.*, 2014, **23**, 207–212.
- 37 H. Li, W. Li, L. Ma, W. Chen and J. Wang, *J. Alloys Compd.*, 2009, **471**, 442–447.
- 38 C. Zhao, J. Kong, X. Yao, X. Tang, Y. Dong, S. L. Phua and X. Lu, *ACS Appl. Mater. Interfaces*, 2014, **6**, 6392–6398.
- 39 X. Wang, Z. Zhang, Y. Chen, Y. Qu, Y. Lai and J. Li, *J. Alloys Compd.*, 2014, **600**, 84–90.
- 40 K. Chang and W. Chen, *Chem. Commun.*, 2011, **47**, 4252–4254.
- 41 L. Zhang and X. W. Lou, *Chem.–Eur. J.*, 2014, **20**, 5219–5223.
- 42 C. Feng, J. Ma, H. Li, R. Zeng, Z. Guo and H. Liu, *Mater. Res. Bull.*, 2009, **44**, 1811–1815.